18. Dehdashti F, Anderson CJ, Trask DD, et al. Initial results with PET imaging using copper-64-labeled TETA-octreotide in patients with carcinoid tumor [Abstract]. *J Nucl Med* 1997;38:103P.
19. Longnecker DS, Lilja HS, French J, Kuhlmann E, Noll W. Transplantation of azaserine-induced carcinomas of pancreas in rats. *Cancer Lett* 1979;7:197–202.
20. Raynor K, Reisine T. Analogs of somatostatin selectively label distinct subtypes of somatostatin receptors in rat brain. *J Pharm Exp Ther* 1989;251:510–517.
21. Munson PJ, Rodbard D. LIGAND: a versatile computerized approach for characterization of ligand binding systems. *Anal Biochem* 1980;107:220–239.
22. Cutler PD, Schwarz SW, Anderson CJ, et al. Dosimetry of copper-64-labeled monoclonal antibody 1A3 as determined by PET imaging of the torso. *J Nucl Med* 1995;36:2363–2371.
23. Taylor JE, Theveniau MA, Bashirzadeh R, Reisine T, Eden PA. Detection of somatostatin receptor subtype 2 (SSTR2) in established tumors and tumor cell lines: evidence for SSTR2 heterogeneity. *Peptides* 1994;15:1229–1236.
24. Breeman WAP, Kwekkeboom, DJ, Kooij PPM, et al. Effect of dose and specific activity on tissue distribution of indium-111-pentetreotide in rats. *J Nucl Med* 1995;36:623–627.
25. Philpott GW, Schwarz SW, Anderson CJ, et al. RadioimmunoPET: detection of colorectal carcinoma with positron-emitting copper-64-labeled monoclonal antibody. *J Nucl Med* 1995;36:1818–1824.
26. Philpott GW, Dehdashti F, Schwarz SW, et al. RadioimmunoPET (MAb-PET) with copper-64-labeled monoclonal antibody (MAb 1A3) fragments [F(ab')2] in patients with colorectal cancers [Abstract]. *J Nucl Med* 1995;36:9P.
27. Apelgot S, Coppey J, Gaudemer A, et al. Similar lethal effect in mammalian cells for two radioisotopes of copper with different decay schemes, copper-64 and copper-67. *Int J Radiat Biol* 1989;55:365–384.
28. Buchegger F, Pfister C, Fournier K, et al. Ablation of human colon carcinoma in nude mice by ^{131}I-labeled monoclonal anti-carcinoembryonic antigen antibody $F(ab')_2$ fragments. *J Clin Invest* 1989;83:1449–1456.
29. Kwa HB, Verhoeven AHM, Storm J, Vanzandwijk N, Mooi WJ, Hilkens J. Radioimmunotherapy of small cell lung cancer xenografts using iodine-131-labelled anti-Ncam monoclonal antibody 123c3. *Cancer Immunol Immunother* 1995;41:169–174.
30. Buchegger F, Rojas A, Delaloye AB, et al. Combined radioimmunotherapy and radiotherapy of human colon carcinoma grafted in nude mice. *Cancer Res* 1995;55: 83–89.
31. Meredith RF, Khazaeli MB, Liu T, et al. Dose fractionation of radiolabeled antibodies in patients with metastatic colon cancer. *J Nucl Med* 1992;33:1648–1653.
32. DeNardo GL, DeNardo SJ, O'Grady LF, Levy NB, Adams GP, Mills SL. Fractionated radioimmunotherapy of B-Cell malignancies with ^{131}I-Lym-1. *Cancer Res (suppl)* 1990;50:1014s–1016s.
33. Krenning EP, Kooij PPM, Pauwels S, et al. Somatostatin receptors: scintigraphy and radionuclide therapy. *Digestion* 1996;57(suppl 1):57–61.
34. Andersson P, Forssell-Aronsson E, Johanson V, et al. Internalization of indium-111 into human neuroendocrine tumor cells after incubation with indium-111-DTPA-D-Phe^1-octreotide. *J Nucl Med* 1996;37:2002–2006.
35. Duncan JR, Stephenson MT, Wu HP, Anderson CJ. Indium-111-diethylenetriaminepentaacetic acid-octreotide is delivered in vivo to pancreatic, tumor cell, and hepatocyte lysosomes. *Cancer Res* 1997;57:659–671.
36. Sharkey RM, Pykett MJ, Siegel JA, Alger EA, Primus FJ, Goldenberg DM. radioimmunotherapy of the GW39 human colonic tumor xenograft with I-131-labeled murine monoclonal antibody to carcinoembryonic antigen. *Cancer Res* 1987;47:5672–5677.
37. Blumenthal RD, Sharkey RM, Kashi R, Goldenberg DM. Comparison of therapeutic efficacy and host toxicity of two different ^{131}I-labelled antibodies and their fragments in the GW-39 colonic cancer xenograft model. *Int J Cancer* 1989;44:292–300.

Evaluation of the Detectability of Breast Cancer Lesions Using a Modified Anthropomorphic Phantom

Niraj K. Doshi, Mario Basic and Simon R. Cherry

Crump Institute for Biological Imaging and Department of Molecular and Medical Pharmacology, University of California at Los Angeles School of Medicine, Los Angeles; and Radiology Support Devices, Inc., Long Beach, California

During the development and characterization of imaging technology or new imaging protocols, it is usually instructive to perform phantom experiments. Often, very simplified forms of the realistic patient anatomy are used that may be acceptable under certain conditions; however, the implications for patient studies can be misleading. This is particularly true in breast and axillary node imaging. The complexities presented by the anatomy, variable object scatter, attenuation and inhomogeneous distribution of activity in this upper thoracic region provide a significant challenge to the imaging task. **Methods:** A tissue-equivalent anthropomorphic phantom of the thorax (Radiology Support Devices, Inc., Long Beach, CA) containing fillable cavities and organs was modified for the studies. The phantom was filled with realistic levels of FDG activity and scanned on a Siemens ECAT HR+ whole-body PET scanner. Breast attachments containing 2.0- and 2.55-cc lesions with lesion-to-background ratios of 5:1 and 7:1, respectively, were imaged. Scatter and attenuation effects were analyzed with various experimental setups. A lymph node experiment and a multibed position whole-phantom scan also were performed to illustrate the extent to which the phantom represents the human thorax. **Results:** Regions of interest were drawn on the lesions as well as the background breast tissue in all studies. It was found that the signal-to-noise ratio decreased 65% when a more realistic phantom (lesions plus breasts plus thorax, all containing activity) was used, as compared to a simple phantom (lesions plus breasts containing activity; no thorax), due to the effects of increased scatter and attenuation. A 23% decrease in the contrast also was seen from the scan of the more realistic phantom due to surrounding activity from nearby organs such as the heart, as well as an increase in the volume of attenuating media. **Conclusion:** This new phantom allows us to more realistically model the conditions for breast and lymph node imaging, leading to preclinical testing that will produce results that better approximate those that will be found in vivo. The phantom will be a valuable tool in comparing different imaging technologies, data collection strategies and image reconstruction algorithms for applications in breast cancer using PET, SPECT or scintimammography systems.

Key Words: phantom; fluorodeoxyglucose PET; breast cancer; breast; lymph nodes

J Nucl Med 1998; 39:1951–1957

It was predicted that 184,300 new invasive cases of breast cancer among women in the U.S. would be diagnosed in 1996 (*1*). Breast cancer is the second leading cause of cancer death in women. Currently, mammography and physical breast examination are the two most effective techniques available for screening potential breast cancer patients.

To improve the quality of care and management of breast cancer patients, in conjunction with screening mammography and other established techniques, there has been a large impetus toward the development of new techniques, altered paradigms and dedicated imaging systems for breast cancer. Scintimammography, lymphoscintigraphy and positron emission mammography, as well as other dedicated imaging techniques and

Received Dec. 8, 1997; revision accepted Feb. 12, 1998.

For correspondence or reprints contact: Niraj K. Doshi, MS, Crump Institute for Biological Imaging, Department of Pharmacology, 700 Westwood Plaza, A-236 JLNRC, Los Angeles, CA 90095-1770.

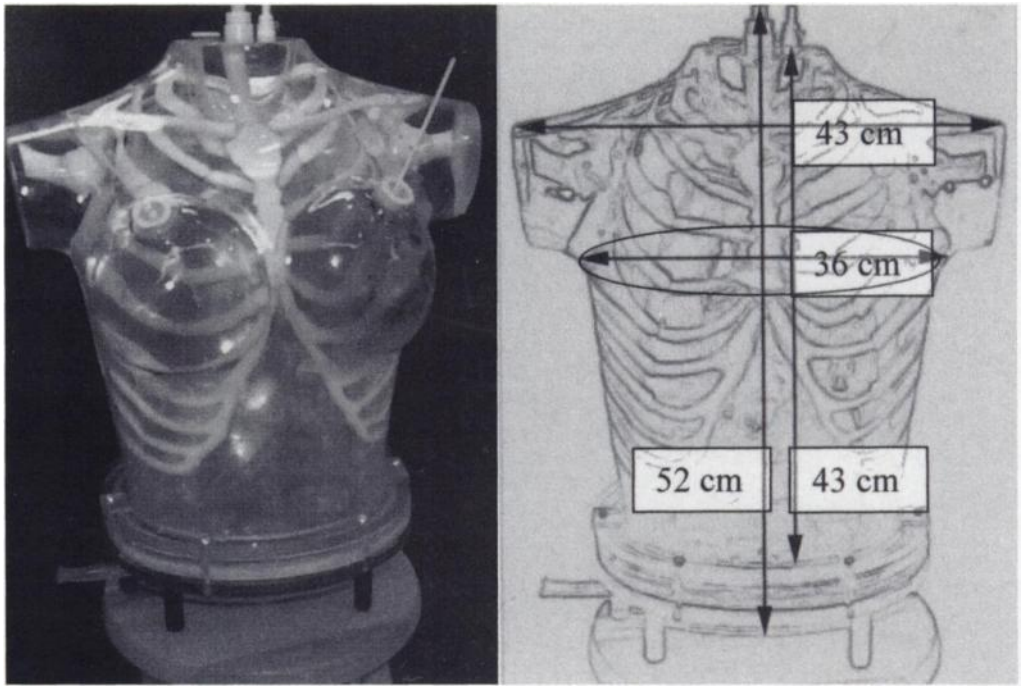

FIGURE 1. A picture and schematic representation of the anthropomorphic phantom. The schematic diagram (Right) also contains various physical measurements of the phantom.

systems, are currently being developed to aid in the fight against breast cancer (*2–10*).

The development and characterization of these new systems or protocols usually is performed with the aid of a phantom. The phantoms generally used are quite simple, in the form of a cylinder with spherical lesions (*6*) or a rectangular box with rod sources (*4*). The use of these simplified phantoms may, however, lead to misleading results in many circumstances. Lesions or objects of interest that can be seen clearly with a simple phantom, with little scattering or attenuating media and a restricted distribution of activity, may not be visualized as clearly in a realistic scenario. An imaging device that has relatively poor energy resolution, timing resolution and counting rate performance may give good images of a simple phantom but very poor images when faced with a more realistic and challenging imaging environment.

The purpose of this study was to develop and implement a more realistic phantom for breast and axillary node imaging as well as to demonstrate the significant role of scatter and attenuation in lesion detectability using PET. Both simple and more realistic phantoms were used to assess the effects of scatter, attenuation and the contribution of activity from adjacent organs (such as the heart and liver) to the breast, lymph nodes and lesions within the breasts.

MATERIALS AND METHODS

Phantom

A fully tissue-equivalent anthropomorphic phantom of the human thorax (Radiology Support Devices Inc., Long Beach, CA.) was modified for the studies. The thoracic cavity and the breast attachments were molded from human models. The phantom is constructed with tissue-equivalent material with appropriate linear attenuation coefficients. Modifications to the phantom included the addition of channels drilled in the axillary regions to allow the simulation of lymph nodes using small capsules containing activity. There are four individual channels drilled in both axillary regions with a diameter of 1 cm, ranging in length from 2 to 4 cm. Thus, variously sized axillary nodes can be placed in any one of the channels, simulating lymph node metastases. Another modification was the development of breast molds in both supine and prone geometry that can be attached directly to the chest with ports for lesions and a cavity for background breast activity. In addition, the phantom contains fillable cavities, accurately representing the geometry and location of the heart, liver and thoracic space, allowing simulation of realistic tissue uptake characteristics. Various sized lesions may be introduced in the breast, axilla, intermammary and supraclavicular regions to simulate breast cancer patients. The dimensions of the phantom are realistically modeled after humans (Fig. 1). Table 1 lists the volumes of the different cavities and organs available for use with the phantom to model human activity distributions realistically. A variety of other lesion sizes may be easily created by the user.

Attenuation Validation

To confirm the tissue equivalency of the various components of the phantom at 511 keV, several narrow-beam geometry linear attenuation measurements were performed.

In the measurements, a ^{18}F point source was placed behind a set of lead bricks that served to collimate the beam with a 10-cm-long × 0.7-cm-wide slit. A single 2 × 2 × 20-cm^3 lutetium oxyorthosilicate crystal was coupled to a photomultiplier tube to serve as the photon detector. The distance between the source and the proximal face of the lutetium oxyorthosilicate crystal was 40 cm. Cylindrical samples of the various phantom materials, such as cortical and spongiosa bone, soft tissue and lung tissue, were each placed on the opposite side of the source adjacent to the lead bricks. A sample of 93.5% pure aluminum (2024-T3) also was measured as a reference to confirm the accuracy of the experimental setup.

TABLE 1
Volumes of Structures and Cavities Used with Phantom

Cavity/structure	Volume (ml)
Thoracic cavity	8200
All heart chambers	286
Liver	998
Left and right lungs	878 and 1153
Supine left and right breasts	514 and 456
Prone left and right breasts	521 and 500
Breast lesions	2.0 and 2.5
Lymph nodes	1.0, 2.1, 2.2

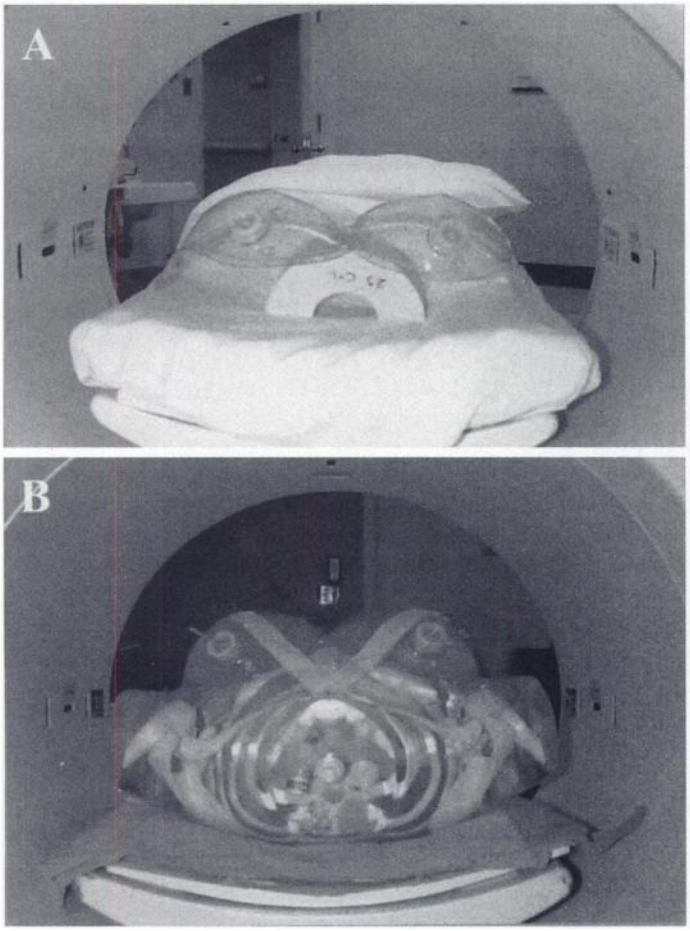

FIGURE 2. (A) The breasts and lesions in the supine position in the gantry of the PET scanner as scanned in lesion Experiment 1. (B) The position of the phantom as scanned in lesion Experiments 2 and 3, as well as the lymph node experiment.

Three measurements were taken for 1 min each and averaged. Thereafter, the sample thickness was increased by adding another piece of the same material juxtaposed to the first piece. Again, three measurements were taken for 1 min each and then averaged. In total, the sample thickness was varied from 2 to 8 cm. A background measurement in which no radioactive source was present was made and then subtracted from all other measurements. A measurement with no attenuator present in the path of the narrow beam also was made.

On completing the measurements, the linear attenuation coefficient for the various tissues was calculated by linear regression on a logarithmic plot of the data. The slope of the line was the linear attenuation coefficient.

Whole-Body PET Scanner Experiments

Lesion Imaging Experiments. Three different experiments were performed on a Siemens/CTI ECAT EXACT HR+ (Knoxville, TN) PET scanner. The three experiments were used to determine the role of object scatter, attenuation and activity distribution in defining image signal-to-noise ratio (SNR) and contrast with both the simple and realistic phantoms.

In Experiment 1, only the supine geometry breast molds containing single lesions each were scanned. The left breast was 514 cc containing a 2.55-cc lesion. The right breast was 456 cc and contained a 2.0-cc lesion. The lesion-to-background activities were 7:1 and 5:1 for the left and right breasts, respectively. The activity ratios were verified by taking samples and measuring them in a well counter. The breasts containing the lesions were placed in the supine position during the scanning procedure (Fig. 2A) and were not attached to the rest of the phantom. This setup allowed the closest simulation of a simple phantom, in which the scatter and attenuation from the rest of the thorax is ignored. Also, the activity distribution is restricted to that contained in the breasts and lesions alone, eliminating any contributions from activity outside the area of interest.

TABLE 2
Concentration Values for Various Tissues as Determined from Real Patient Data

Tissue/organ	Concentration (μCi/cc) ± s.d.
Lesion	0.18 ± 0.02
Myocardium	0.13 ± 0.02
Liver	0.11 ± 0.01
Breast	0.05 ± 0.01
Thoracic cavity	0.05 ± 0.01

In Experiment 2, the same breast molds and lesions used in Experiment 1 were attached to the thorax. The thorax contained the lungs, heart and liver and was filled with cold water without any radioisotope. Again, the phantom was placed in the supine position in the scanner as shown in Figure 2B. In this protocol, an assessment of the contribution of attenuation and scatter due to the presence of the thorax and its respective organs could be made. The activity distribution remained identical to that in Experiment 1.

In Experiment 3, the thoracic cavity, heart and liver were now all filled with realistic activity concentrations (Fig. 2B). This scanning setup provided the most complex and closest simulation to that which occurs while scanning a real patient. Thus, in this protocol, the complex geometry, attenuation, scatter and activity distribution were all replicated as closely as possible to a real human's characteristics.

To fill the phantom and its various components with realistic activity levels, four breast cancer patient scans from whole-body PET studies were obtained to extract the appropriate data. Regions of interest (ROIs) were drawn around the various tissues of interest, such as the breast lesion, breast tissue, heart, liver and background thoracic cavity using commercial software (CAPP; Clinical Applications Programming Package, Siemens/CTI, Knoxville, TN). The ROI values were converted to activity concentrations in units of μCi/cc for each tissue or organ (Table 2).

Scanning Protocol. All the experiments followed a similar scanning protocol. The phantom was filled with ^{18}F-fluorodeoxyglucose (FDG) solution as described for each experiment, based on values in Table 2. A two-dimensional PET scan was acquired with the breasts centered within the 15-cm axial field of view with the phantom in a supine position. A 60-min emission scan was taken immediately after all the components of the phantom were filled and assembled together. A 20-min transmission scan was taken the following morning, without the phantom being moved, allowing all of the activity to have decayed more than five half-lives. Filtered backprojection was used for reconstructing the 63 image planes using a Shepp filter with a roll-off frequency equal to one-half the Nyquist frequency. No axial smoothing was performed on the images. The images were reconstructed at the highest resolution to accentuate the SNR and contrast differences between the experimental conditions and to minimize confounding factors such as partial volume effects. All scans were performed on the same scanner and identical scanning conditions were maintained.

Qualitative Imaging Experiments. To test the ability of the phantom to simulate lymph node involvement, the entire phantom, including the supine geometry breast molds, heart, liver and thoracic cavity, were all filled with realistic levels of activity. A 1.0-cc lesion was placed in the mediastinal area, on the left side, posterior to the sternum and between the second and third ribs. A

2.1-cc lesion was placed in the left axillary region, 2.0 cm below the surface. Both lesions were at 7:1 lesion-to-background activity, using the activity values listed in Table 2. The phantom was positioned as shown in Figure 2B. The same scanning protocol, as described above, was used for the lesion experiments.

A modified multibed position whole-phantom scan also was conducted. The entire phantom was filled with activity according to values listed in Table 2. Lesions of 2.0 and 2.55 cc were inserted in the right and left breasts, respectively, as was done in the lesion experiments. The two lymph nodes also were placed, as described above, in the mediastinal and left axillary regions. A third lymph node, 1.6 cc in volume, was added in the right axillary region, 1.5 cm below the surface. The scan protocol was a modified version of the typical whole-body scanning protocol used for clinical patients at the University of California at Los Angeles. Essentially, four bed positions were scanned with a four-plane overlap between bed positions. A 20-min emission scan was acquired for the first bed position, 35 min for the second, 50 min for the third and 65 min for the fourth bed position. The increase of 15 min in scanning time for each bed position compensated for the decrease in counts due to radioactive decay. A 20-min transmission scan was performed for each bed position. Hanning filters with 0.44 and 0.42 Nyquist frequency cutoffs were used for the radial and axial directions, respectively.

Signal-to-Noise Ratio and Contrast Analysis

After the scans were completed and the data were acquired, the images were analyzed using ROI analysis. The ROIs were defined over the lesion and over background tissue using the CAPP software. The ROI values were imported into Microsoft Excel (Microsoft Corp., Redmond, WA). The SNR and contrast were computed for the different experiments.

The SNR was assumed to be proportional to the quotient of the mean ROI values of the lesion divided by the mean of the standard deviation of the background breast region. The lesion ROIs were drawn on all the planes that contained lesion activity in such a fashion as to include all pixels containing ~70% of the maximum pixel value. The background tissue ROIs were drawn on several planes of the image volume, on the image slices of the breasts not containing any lesion volume, usually 10 planes above the plane where the lesion activity starts.

The contrast was calculated by taking the mean ROI value for the lesion minus the mean ROI value of the background, then dividing by the mean ROI value for the lesion. Again, the same procedure for ROI drawing was used as described above.

RESULTS

Attenuation Validation

The measured linear attenuation coefficients for the various tissue samples at 511 keV were close to real human tissue values as quoted by Hubbell (*11*). Looking at a few examples, the measured attenuation coefficient for cortical bone was 0.16 cm^{-1}, whereas Hubbell quotes it as 0.17 cm^{-1} for 511 keV. The value for soft tissue from Hubbell is 0.10 cm^{-1}, which is fairly close to the value of the phantom's soft tissue sample, which was 0.11 cm^{-1}. Finally, the value of aluminum as listed in the text is 0.23 cm^{-1}, compared to 0.24 cm^{-1} from the measurement. The complete results of the measurements are listed in Table 3. A group from St. Joseph's Health Center (London, Ontario, Canada) has previously validated the tissue equivalency of the phantom at 140 keV (*12*) for use with ^{99m}Tc-labeled tracers.

TABLE 3
Measured Linear Attenuation Coefficients for 511-keV Photons

Sample	Phantom linear attenuation coefficients (cm^{-1}) ± s.d.
Cortical bone	0.156 ± 0.004
Spongiosa bone	0.088 ± 0.002
Soft tissue	0.110 ± 0.009
Lung tissue	0.039 ± 0.002
Aluminum (reference)	0.240 ± 0.025

Whole-Body PET Scanner Experiment Results

Lesion Imaging Experiments. The images of the various breast lesion experiments are presented in Figure 3. The differences in image quality due to the variation in attenuation, scatter and activity distribution between the experimental setups are readily seen.

The image from Experiment 1 (Fig. 3A) is less noisy and has better contrast than the other images. The breasts and lesions are clearly resolved. The average SNR of the left and right breasts was measured to be 14.63. The average contrast was found to be 0.71.

In Experiment 2 (Fig. 3B), the average SNR and contrast were 8.74 and 0.65, respectively, a 40.2% decrease in SNR and an 8.7% decrease in contrast in comparison to Experiment 1. Thus, with the addition of the thorax filled with water and no activity, an appreciable decrease in SNR and contrast was noted. The water-filled thorax scatters and attenuates the photons from the activity-filled breasts and lesions, thereby diminishing the total number of true coincidence events detected. An almost 3-fold decrease in net trues is seen from Experiment 1 to Experiment 2 (Table 4), leading to a diminished SNR. Because of the presence of the thorax there are many more scattered photons. The detection of these scattered photons provides a randomized, indistinct background in the images, which leads to a reduction in contrast.

In Figure 3C, the thorax, lungs, myocardium and breasts are easily differentiated. However, the contrast between the lesions and the background tissue activity is much less evident in comparison to Experiment 1. A notable downward trend in SNR and contrast was seen both in the images and in the numbers, as shown in the graphs in Figure 4. In Experiment 3, when the thorax was filled with realistic levels of activity, a 65.3% decrease in SNR and a 22.7% decrease in contrast were noted as compared to Experiment 1. In Experiment 3, the contribution from activity from organs outside the area of interest, such as the heart and liver, increased the total number of singles detected in the field of view. The randoms rate increased with the square of the singles rate. The randoms fraction increased to 7.6% in Experiment 3, whereas it was only 0.8% in Experiment 1 and 1.2% in Experiment 2 (Fig. 5). This increase in randoms ultimately leads to an increase in the noise because the true coincidence events are corrected for randoms. Because the number of true coincidence events is equal to the total number of prompts minus the total number of randoms, the process of correcting for the random events adds noise to the image. Also, with an increase in singles rate, the scanner dead time increases, thereby reducing the total number of true coincidence events detected from the breast region, decreasing the signal. Thus, with an increase in noise and a decrease in signal, there is a further dramatic decrease in the SNR.

The decrease in contrast is to be expected because the activity outside the breast region, primarily from the heart and liver, can scatter into the breast region. The detection of these additional scattered photons provides a very uniform, indistinct background, thereby decreasing the overall contrast.

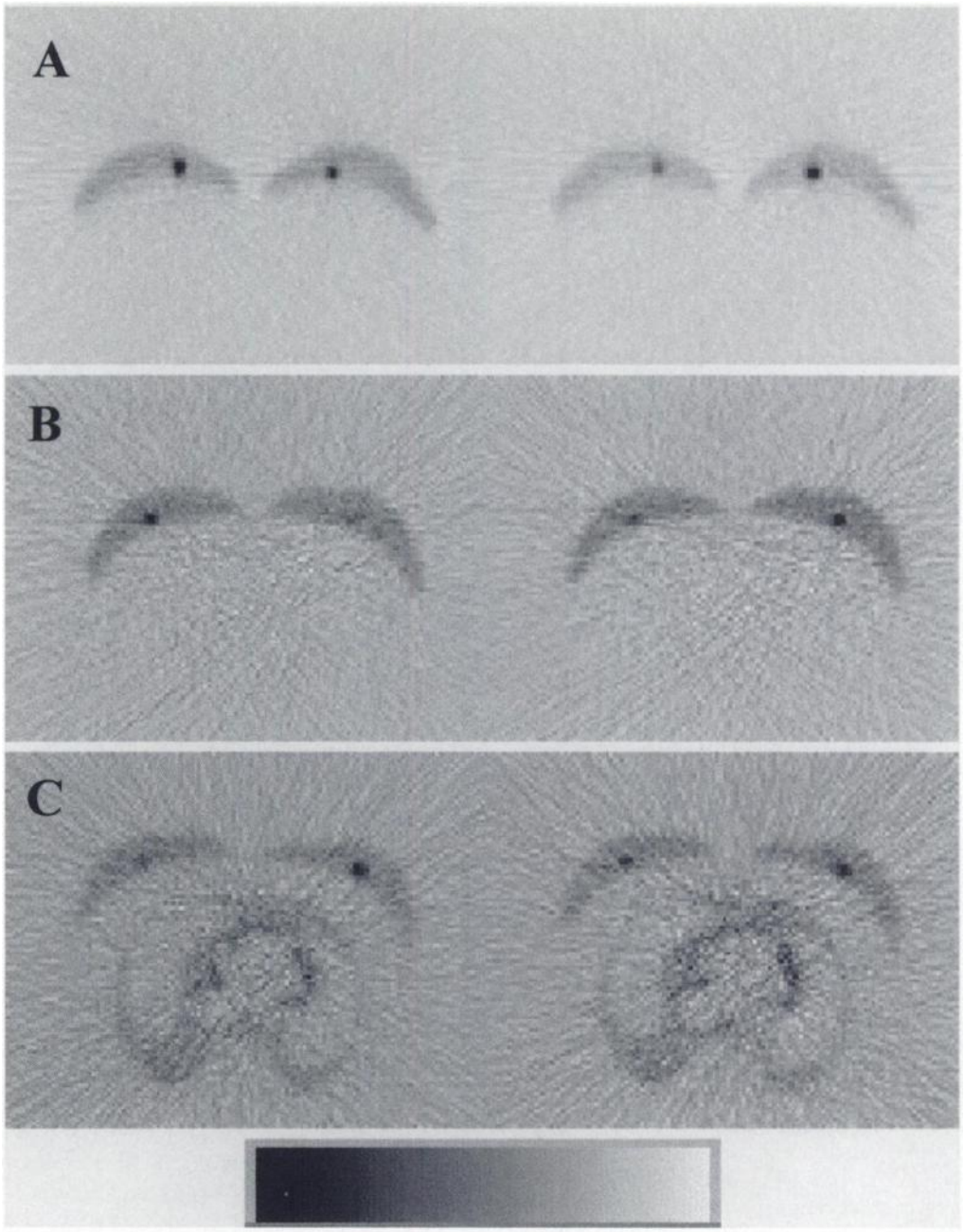

FIGURE 3. (A) Images from lesion Experiment 1 (imaging breasts and lesions only). (B) Images from lesion Experiment 2 (breasts and lesions attached to a water-filled thorax). (C) Images from lesion Experiment 3 (breasts and lesions attached to an activity-filled thorax). Note the change in image quality, even though the amount of radioactivity in the breast and lesions is constant throughout all three experiments.

Qualitative Imaging Experiments. In Figure 6, a representative image of the phantom in a horizontal slice is shown. From the image, the mediastinal and axillary nodes are clearly discriminated in relation to the breasts, heart, lungs and thoracic space. No background activity surrounding the axillary node was seen because of the physical structure of the phantom. The internal thoracic cavity of the phantom is somewhat dome-shaped near the clavicular region, and thus, no background activity is present in the axilla itself. In contrast, the mediastinal node is completely surrounded by activity from the thoracic space.

In Figure 7, coronal and sagittal projection views of the whole thoracic phantom filled with FDG is shown. To show the various organs and cavities in a single view, several slices of the original image file were added. Organs and lesions such as the lymph nodes, myocardial wall, liver and lungs are distinct, and the similarity to real human studies can be appreciated.

TABLE 4
Some of the Relevant Values from Three Breast Lesion Experiments

	Net trues* (cps)	Randoms (cps)	Singles (cps)
Experiment 1	537	5	206,260
Experiment 2	197	2	155,235
Experiment 3	472	36	580,665

*The net trues are corrected for randoms.

DISCUSSION

In the first experimental setup, a simple phantom was simulated by using only the breast molds and lesions. This provided the smallest amount of scattering and attenuating medium. It also closely resembled what several other groups use in terms of phantoms, such as boxes or cylinders, in their studies. With this setup, the best SNR and contrast were observed. The lesions were easily detectable.

In the second experiment the thorax, heart and liver, filled with cold water, were added. Essentially, the contribution of

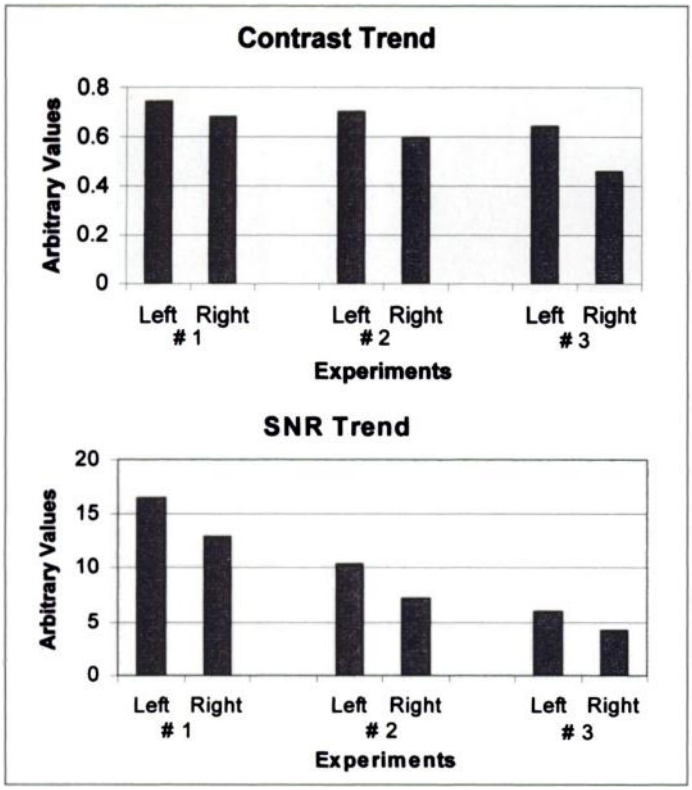

FIGURE 4. Graphs of the contrast and SNR trends for each of the three lesion experiments. There was a considerable decrease in both contrast and SNR as scattering material and activity outside the breasts was added.

object scatter and increased attenuation due to the rest of the body on the SNR and contrast were to be assessed. Both figures of merit decreased, as expected, with the increase in object scatter and attenuation.

In the third setup, the thorax, heart and liver were all filled with realistic activity levels. This was the closest achievable simulation of breast cancer patients, barring the inclusion of the axillary nodes. This more realistic scenario produced the worst SNR and contrast. However, because this is a fairly close simulation of scanning a real breast cancer patient, it provides the most accurate means of determining the scanner's performance characteristics in evaluating real patients.

In the imaging experiments, the flexibility of the phantom to provide unique datasets was demonstrated. Because lymph nodes can be placed in various anatomical locations, fairly realistic images simulating breast cancer patients with lymph

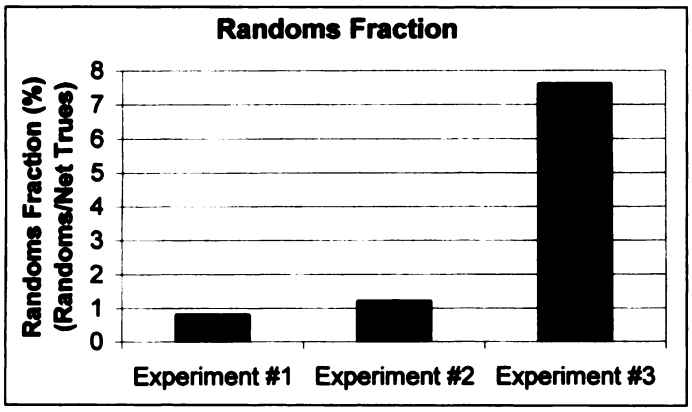

FIGURE 5. A graph representing the randoms fraction as the randoms-to-true coincidence events ratio. With the addition of the activity-filled thorax in lesion Experiment 3, a dramatic increase in the singles counting rate and, therefore, the randoms counting rate was seen.

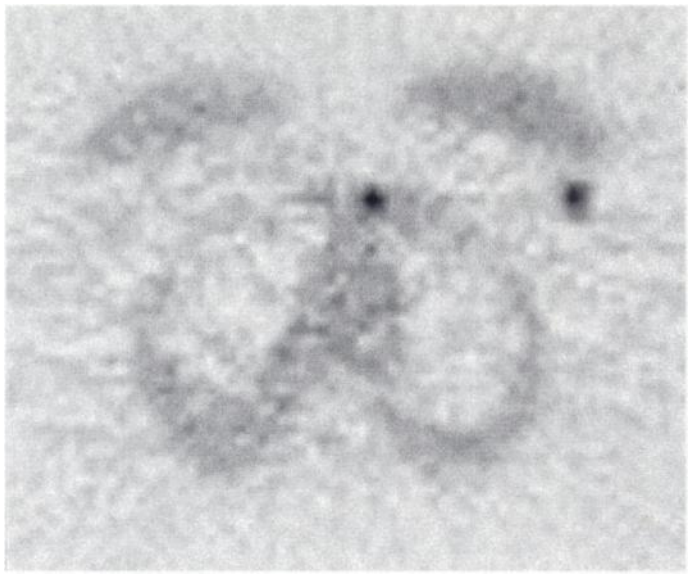

FIGURE 6. Image of the lymph node experiment. A horizontal section showing the mediastinal (1.0-cc) and axillary (2.1-cc) nodes. The imaging protocol used was the same as that used for the lesion experiments. The lesion-to-background ratio was 7:1.

node metastases are obtained, types of images that are difficult to obtain with simple phantoms. The thoracic images provide a good representation of the phantom and its potential uses across multiple modalities. Because the phantom is composed of tissue equivalent material and it contains various realistic, fillable organs and cavities, a plethora of radioisotope uptake scenarios can be simulated, allowing an experimental setup that is fairly close to real patient imaging. The phantom's ability to more closely simulate the scatter and attenuation properties of real human thoraxes in comparison to simple phantoms makes it a unique imaging tool.

Understanding of the important roles of object scatter, attenuation and activity distribution in determining image quality for a dedicated nuclear medicine imaging system designed for breast and axillary region imaging is crucial. Retrospectively, if a simple phantom, such as that delineated in Experiment 1, was used to characterize a new system or new imaging protocols, inaccurate and misleading results regarding lesion detectability would be obtained. The breast and axillary region of the thorax is composed of a variety of tissue types with varying attenuation coefficients. The geometry of the region also is very complex. A simple phantom does not provide a realistic activity distribution, scatter or attenuation environment to accurately account for the level of degradation of SNR and contrast as would occur in a real patient. This would ultimately lead to incorrect images with favorable SNR and contrast, leading the researcher to believe that the system's performance was better than it would be when used clinically. In particular, these studies demonstrate that the performance of the imaging system in terms of energy resolution, timing resolution, counting rate performance and out-of-field activity shielding will be critical for achieving high-quality images in a realistic imaging environment. However, simple phantoms are quite useful for other means, such as validating Monte Carlo simulations, or when an isolated portion of human anatomy is to be imaged that is not of complex geometry or composed of variegated tissue types. The modified anthropomorphic phantom allows a close simulation of real patient anatomy and, with the correct amount of activity loaded into the appropriate cavities and organs, the radioisotope uptake can be closely imitated, as well.

This multimodality anthropomorphic phantom allows the

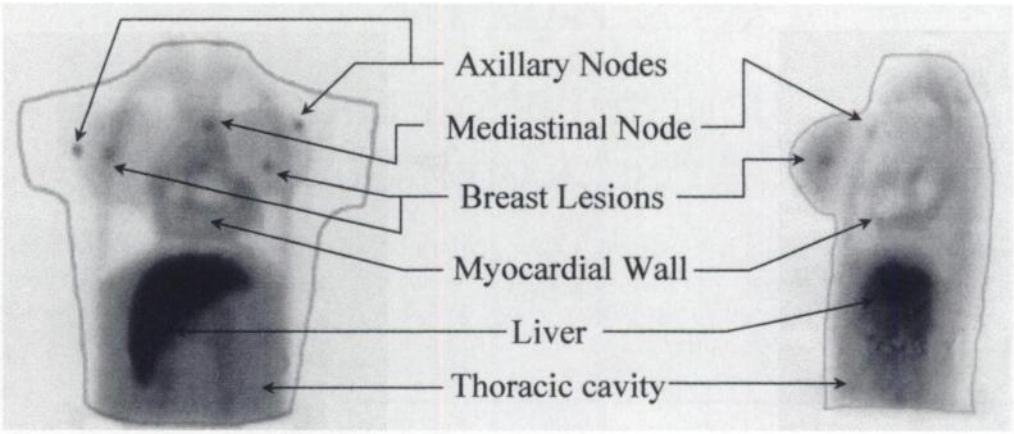

FIGURE 7. A coronal and sagittal projection view of the thoracic phantom filled with FDG and scanned on a whole-body PET scanner. Various organs and lesions are distinguished in the above images. The external outlines of the phantom were drawn artificially onto the images.

close simulation of breast cancer patient anatomy with respect to the complex geometry of the breast and axillary regions, as well as appropriate radioisotope activity distributions relative to the breast lesions, axillary nodes, breasts, heart, liver and thoracic cavity. It is our intention to use this phantom to assist in the characterization of our dedicated mammary and axillary node PET imaging system in the near future.

CONCLUSION

Signal-to-noise ratio and contrast decrease with the addition of a thorax containing organs filled with realistic activity levels. Object scatter, attenuation and the activity distribution play a crucial role in breast lesion detectability. Thus, the use of a realistic phantom is vital in characterizing new nuclear medicine technology or protocols for breast imaging. The development of this multimodality phantom provides an excellent means of simulating nuclear medicine studies of the breast and axillary regions, both of which are located in an area of the body with complex geometry and multiple tissue types. This phantom will be an invaluable tool in comparing different imaging technologies, data collection strategies and image reconstruction algorithms for applications in breast cancer using PET, SPECT or scintimammography systems. The unique datasets also can be used to run receiver operating characteristic studies to assess and to compare various imaging modalities, algorithms or techniques.

ACKNOWLEDGMENTS

We thank Ron Sumida, Larry Pang, Francine Aguilar, Der-Jenn Liu, Sumon Wongpiya, Priscilla Contreras and Abdel Boutefnouchet for assisting with the scans; Magnus Dahlbom for assistance with CAPP; and Thomas Farquhar for helpful discussions. A poster of this paper was presented at the 44th Annual Meeting of the Society of Nuclear Medicine, held in San Antonio, TX in 1997. This work was supported by the U.S. Army Grant DAMD17-96-1-6200 and California Breast Cancer Research Training Grant 513408-18071.

REFERENCES

1. American Cancer Society. Cancer facts and figures: 1996. Atlanta: American Cancer Society; 1996.
2. Adler DD, Wahl RL. New methods for imaging the breast: techniques, findings, and potential. *Am J Roentgenol* 1995;164:19–30.
3. Khalkhali I, Mena I, Diggles L. Review of imaging techniques for the diagnosis of breast cancer: a new role of prone scintimammography using technetium-99m sestamibi. *Eur J Nucl Med* 1994;21:357–362.
4. Thompson CJ, Murthy K, Weinberg IN, Mako F. Feasibility study for positron emission mammography. *Med Phys* 1994;21:529–538.
5. Moses WW, Budinger TF, Huesman RH, Derenzo SE. PET camera designs for imaging breast cancer and axillary node involvement. *J Nucl Med* 1995;36:69P.
6. Freifelder R, Karp JS. Dedicated PET scanners for breast imaging. *Physics in Med and Biol* 1997;42:2463–2480.
7. Steinbach D, Cherry S, Doshi N, et al. A small scintimammography detector based on a 5" PSPMT and crystal scintillator arrays. *IEEE Nucl Sci Symp Med Imag* 1997; Nalcioglu O, ed. CD-ROM paper no. M07–22.
8. Tse NY, Hoh CK, Hawkins RA, et al. The application of positron emission tomographic imaging with fluorodeoxyglucose to the evaluation of breast disease. *Ann Surg* 1992;216:27–34.
9. Hoh CK, Hawkins RA, Glasby J, et al. Cancer detection with whole-body PET using 2-[F-18]-fluoro-2-deoxy-D-glucose. *J Comput Assist Tomogr* 1993;17:582–589.
10. Uren RF, Howman-Giles RB, Thompson JF, et al. Mammary lymphoscintigraphy in breast cancer. *J Nucl Med* 1995;36:1775–1780.
11. Hubbell, JH. Photon mass attenuation and energy-absorption coefficients from 1 keV to 20 MeV. *Int J Appl Radiat Isot* 1982;33:1269–1290.
12. Stodilka RZ, Kemp BJ, Prato FS, Nicholson RL. The importance of bone attenuation in brain SPECT quantification. *J Nucl Med* 1998;39:190–197.